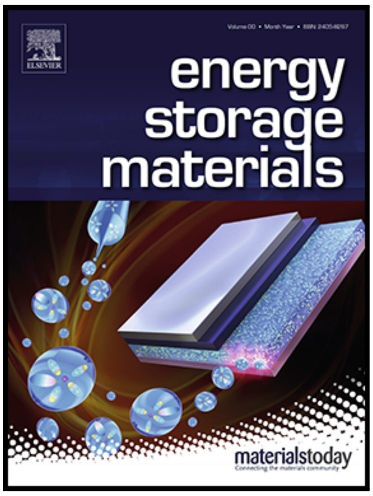

Quantitatively Regulating Defects of 2D Tungsten Selenide to Enhance Catalytic Ability for Polysulfide Conversion in a Lithium Sulfur Battery

Hao-Jie Li , Kai Xi , Wei Wang , Sheng Liu , Guo-Ran Li ,
Xue-Ping Gao

PII: S2405-8297(21)00541-9
DOI: https://doi.org/10.1016/j.ensm.2021.11.024
Reference: ENSM 1933

To appear in: *Energy Storage Materials*

Received date: 18 September 2021
Revised date: 5 November 2021
Accepted date: 14 November 2021

Please cite this article as: Hao-Jie Li , Kai Xi , Wei Wang , Sheng Liu , Guo-Ran Li , Xue-Ping Gao , Quantitatively Regulating Defects of 2D Tungsten Selenide to Enhance Catalytic Ability for Polysulfide Conversion in a Lithium Sulfur Battery, *Energy Storage Materials* (2021), doi: https://doi.org/10.1016/j.ensm.2021.11.024

Quantitatively Regulating Defects of 2D Tungsten Selenide to Enhance Catalytic Ability for Polysulfide Conversion in a Lithium Sulfur Battery

Hao-Jie Li[a], Kai Xi[b], Wei Wang[a], Sheng Liu[a], Guo-Ran Li[a *], and Xue-Ping Gao[a]

[a]*Institute of New Energy Material Chemistry, School of Materials Science and Engineering, Renewable Energy Conversion and Storage Center, Nankai University, Tianjin 300350, China*

[b]*Department of Engineering, University of Cambridge, Cambridge CB3 0FA, United Kingdom*

[*] Correspoding author.
E-mail: guoranli@nankai.edu.cn.

Highlights

- On the basal planes of 2D WSe_2, defects are quantitatively created.
- The relationship among the defects of the 2D material, catalytic ability, and electrochemical performance of lithium sulfur battery are clearly established.
- The optimal S/$WSe_{1.51}$/CNT electrode delivers a high areal capacity of 11.3 mAh cm^{-2}, and outstanding cycle stability with a decay rate of 0.025% during 1000 cycles at 1C rate.
- The effect mechanism of the defects on lithium sulfur battery is revealed deeply.

Abstract

Introducing defects into 2D materials can increase the coordinatively unsaturated sites that are usually also catalytically active sites. How does the level of defects influence catalytic performance and how to take advantage of defects to optimize the 2D materials? In this work, anionic Se vacancies and edge dislocations are regulated in 2D WSe_2 as a model of transition metal dichalcogenide host material for the sulfur cathode. The defective 2D WSe_2 with different W/Se ratios are quantitatively investigated the influence of the defects on enhancing the cathodic process in lithium sulfur (Li-S) batteries. With a moderate level of defects, $WSe_{1.51}$ shows the optimal performance for adsorbing polysulfides, catalysing polysulfides conversion, and promoting liquid-solid transformation, all of which are crucial steps for Li-S battery. The corresponding sulfur cathode delivers a high initial areal capacity of 11.3 mAh cm $^{-2}$, and excellent cycle stability with a decay rate of 0.025% during 1000 cycles at 1C rate.

Even in a pouch cell, the excellent cyclability and flexibility are still available. The results show the feasibility of enhancing the catalytic ability of 2D transition metal dichalcogenide by controlling the level of defects by which a long-cycle and high-energy Li-S rechargeable battery can be achieved.

Keywords: lithium-sulfur battery, 2D material, defect, electrochemistry, catalysis

1. Introduction

Benefit from the high theoritical energy density of 2600 Wh/Kg, lithium sulfur (Li-S) batteries have been widely studied as a potential high-energy alternative for lithium ion batteries [1-4]. The total reaction of lithium sulfur battery is very complicated solid–liquid–solid phase conversion processes involving many sequential steps, in which kinetics of polysulfide conversion in the sulfur cathode is one of the most important factors to determine the final performance of lithium sulfur battery [5-8]. In particular, high sulfur loading in cathodes needed to meet high energy density outputs must demand a fast kinetical conversion of the polysulfide immediates in the electrode reaction, which normally depends on the catalytic effect provided by the host materials of sulfur in the cathodes [9, 10].

Therefore, catalytic ability of host materials for polysulfide conversion has become one of the most concerned issues for lithium sulfur battery in the near fulture. Compared with the carbon-based host materials in the early research of lithium sulfur battery, transition metal composites could provide relatively high catalytic ability due to the interaction between the metal composites and polysulfides [11-14]. Transition metal dichalcogenides (TMDCs) have the characteristic sandwiched configuration of X–M–X (M, transition metal; X, chalcogen) pillared by Vander Waals forces, resulting atomic-scale thickness, direct bandgap, strong spin–orbit coupling and favourable electronic and mechanical properties [15-18]. The lamellar morphology and the good compatibility with polysulfides make TMDCs have great potential to be used as host materials in sulfur cathodes [16, 19-21]. However, as catalytic materials, TMDCs usually provide active sites on the edge planes rather than the basal planes because the basal planes have relatively low surface Gibbs free energy and few coordination unsaturated sites [19, 22-24].

As an effective approach, introducing defects such as site vacancies and dislocations in catalytic materials can raise coordination unsaturated sites that are usually also catalytically active sites. In some cases of Li-S batteries, the vacancies in the polar configuration cause the electron coordination unsaturated to reduce electron transfer energy barrier and enhance electrophilic adsorption [25-30]. It has been demonstrated that the defects in Nb_2O_5 and MoS_2 could significantly enhance the adsorption and catalytic conversion kinetics of polysulfide intermediates [31, 32]. Moreover, acceleration of electron transport from polysulfides to electron-vacancy sites can trigger strong chemical polar-binding performance and improved catalytic kinetics [27, 33-35]. However, owing to the complicated reaction mechnism, it is actually difficult to demonstrate clearly how the defects influence Li-S batteries on electrode process and final electrochemical performance, in particular, quantitatively.

In this work, WSe_{2-x} is used as the host material in sulfur cathode on account of its merits like electronic structure of enhanced spin-orbit coupling (SOC) feature that is helpful for eletron transport, compared with the other TMDCs [15, 16, 36, 37]. In WSe_{2-x}, Se vacancies are generated quantitatively by varying preparation conditions, and the site vacancies can induce the formation of dislocations in basal planes, which leads to the formation of a series of WSe_{2-x} samples with gradient Se defects. The influence of the defects on adsorption of polysulfide and catalytic effect for polysulfide conversion is investigated by theory calculations and experiments. The sample $WSe_{1.51}$ with a moderate number of defects shows the optimal adsorption ability and catalytic ability of polysulfides. With carbon nanotubes (CNTs) as electrical connection, the S/$WSe_{1.51}$/CNT electrode deliveries high capacity and stable cycling for Li-S batteries with a high sulfur areal loading.

2. Results and discussion

2.1 Defect regulation of tungsten selenium

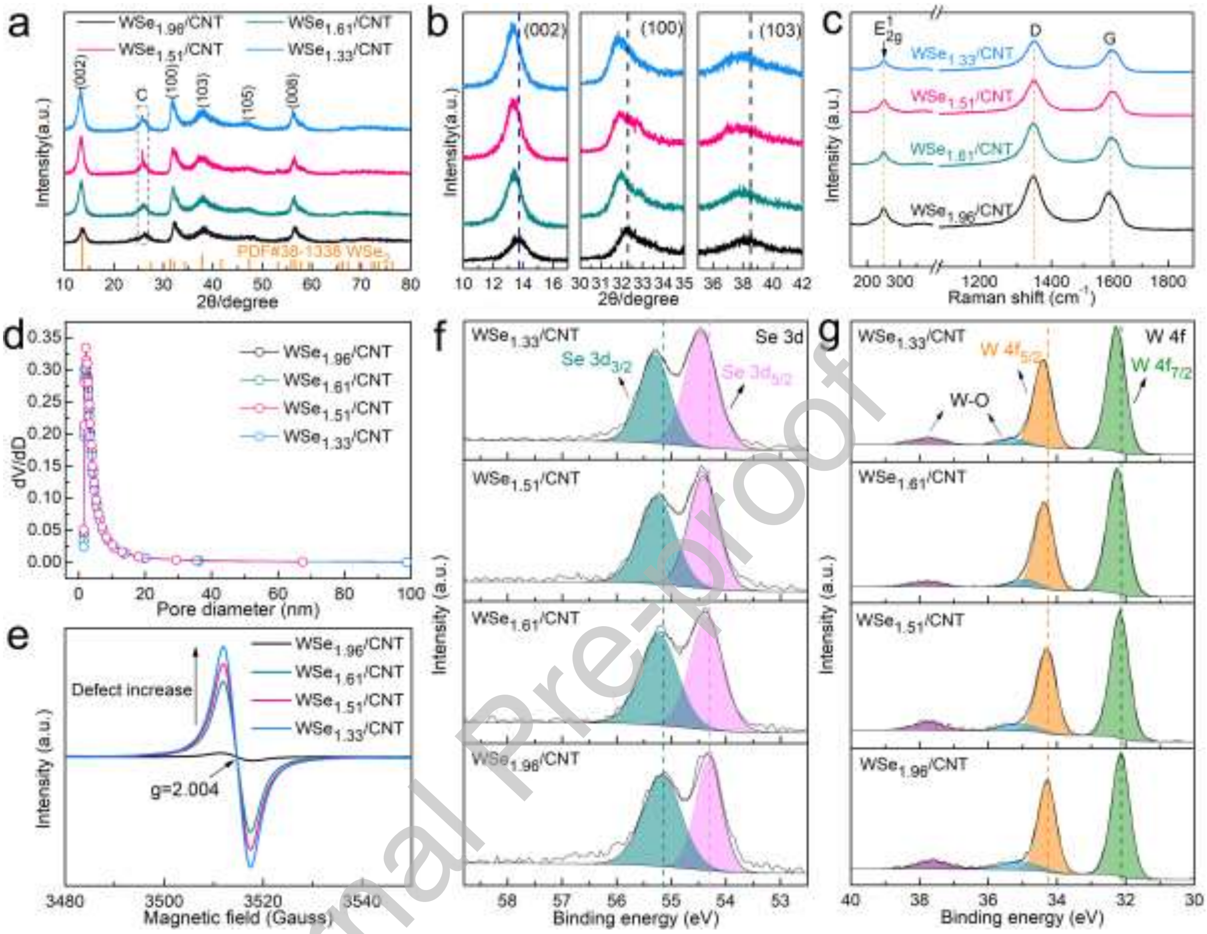

Fig. 1. Characterization of WSe_{2-x}/CNT. (a, b) XRD patterns; (c) Raman spectra; (d) Pore size distribution plots; (e) Electron spin resonance spectra; and (f, g) XPS of Se 3d and W 4f.

The solvothermal method allows to synthesize stoichiometric WSe_2. CNTs as one-dimensional electrically conductive materials are added into the solvent to form finally the three-dimensional interlinked structure like the reported previously (Fig. S1) [38, 39]. With a little change of annealing conditions described in the experimental section, WSe_{2-x} with various amounts of Se vacancies are obtained. According to the determination results of Inductively Coupled Plasma Optical Emission Spectroscopy (ICP-OES), the ratio of W to Se for the as-prepared sample is 1.96, very close to the stoichiometric atomic ration, and the ratios for the three regulated samples are 1.61, 1.51, and 1.33 (Table S1), respectively, marked as $WSe_{1.96}$/CNT, $WSe_{1.61}$/CNT, $WSe_{1.51}$/CNT, and $WSe_{1.33}$/CNT. The X-ray diffraction (XRD) patterns shown in Fig. 1a confirm that all the obtained WSe_{2-x} samples have the same hexagonal structure (PDF#38-1388), and the defect reglution in the designed range has no effect on the basal crystalline phase. However, the comparison of the diffraction peaks of (002), (100) and (103) planes presents a very slight shift to low angle with the increase of defects (Fig. 1b), indicating lattice parameters enlarge marginally due to the more Se vacancies. In the Raman spectra, the peak at 250 cm^{-1} is attributed to E_{2g}^{1} mode of WSe_2, and the peaks located at 1347 and 1589 cm^{-1} are the D band (disorder induced band) and G-band (graphitic band) of carbon, respectively (Fig. 1c) [20, 40, 41]. For all the samples, the peak intensity of the ratio of I_D/I_G for CNT are very close, demonstrating the defect regulation processes make no difference in the side of CNTs [42]. With increase of defects, the pore size distribution of the samples has no obvious change, but the specific surface area has light improvments from 685.1 m^2 g^{-1} for $WSe_{1.96}$/CNT to 761.5 m^2 g^{-1} for $WSe_{1.51}$/CNT (Fig. 1d, Table S2). The ESR results in Fig. 1e indicate clearly the gradual increase of defects from $WSe_{1.96}$/CNT to $WSe_{1.33}$/CNT, in which the ESR signal g=2.004 is correlated to Se-vacancy in WSe_{2-x}, further confirming the quantitative regulation of defects [43, 44]. In addition, in the XPS results, the peaks of Se3d show a gradual shift towards higher binding energy, the position of Se 3d5/2 from 54.31 eV for $WSe_{1.96}$/CNT to 54.48 eV for $WSe_{1.33}$/CNT. This can be understood as a consequenc of W-Se bonds strengthening owing to the lack of Se (Fig. 1f) [26]. Conversely, the regular shift of binding energy also confirms the gradient change of defects. The W4f spectra also show consistent results, except for the two additional peaks at 35 eV and 37.6 eV derived from the inevitable surface oxidation in the XPS measurements (Fig. 1g) [26, 45].

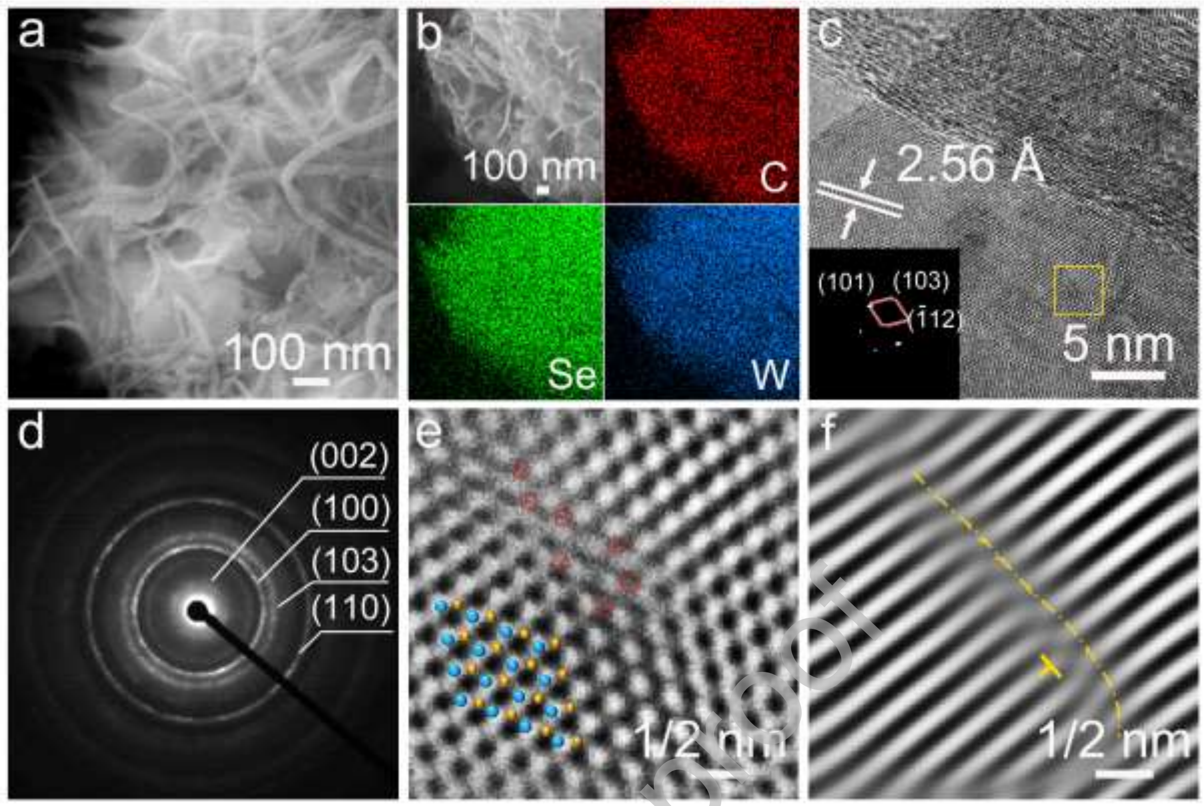

Fig. 2. Morphology and microstructure. (a) The SEM and (b) EDS elemental mapping of $WSe_{1.51}$/CNT. (c) HRTEM images of $WSe_{1.51}$/CNT and the corresponding FFT patterns show that the prepared materials match the crystalline planes of hexagonal-phase WSe_2 (PDF#38-1388). (d) SAED image of $WSe_{1.51}$/CNT. (e, f) the IFFT pattern of the selected area by the yellow rectangle in image (c). (e, in the overlaid crystal models, blue circles represent tungsten atoms, yellow circles represent selenium atoms; red circles represent Se defect; f, yellow mark represent dislocation).

As designed, the SEM images show that 2D WSe_{2-x} and 1D CNTs can form a 3D interlinked structure which is beneficial for loading of sulfur (Fig. 2a and S2). The element mapping from energy dispersive spectroscopy (EDS) of $WSe_{1.51}$/CNT in Fig. 2b verifies that $WSe_{1.51}$ and CNTs are homogeneously composited, and the CNTs mass content is 39.7 wt% (Fig. S3), essentially in agreement with the result determined by the elemental analysis method in Table S1 (40.47 wt%). The TEM images for all the WSe_{2-x}/CNT samples clearly display 2D feature of the few-layer WSe_{2-x} and the contection between WSe_{2-x} and CNTs (Fig. S4). Influenced by the regulated vacancies, the interplanar spacing of (002) basal plane has a gradual increase with the growing of defects (Fig. S5), consistent with the analysis of XRD results. Fig. 2c shows a typical TEM image of $WSe_{1.51}$/CNT, in which the interplannar spacing of 2.56 angstroms corresponds the (103) plane of WSe_2, the inserted Fast Fourier Transform (FFT) pattern and the corresponding selected area electron diffraction (SAED) pattern in Fig. 2d show clearly the diffraction patterns of (002), (100), (103) and (110) planes of hexagonal WSe_2 in $P6_3/mmc$ space group. More importantly, it is found from the Inverse Fast Fourier Transform (IFFT) results based on the selected region in Fig. 2c that, besides the observable atomic point defects (Se vacancies) shown in Fig. 2e, lots of linear defects (edge dislocations) appear in the basal planes of tungsten selenide (Fig. 2f), around which there is a strain field as the atomic bonds have been compressed or stretched. For the near-stoichiometric sample $WSe_{1.96}$/CNT, few Se vacancies and edge dislocations are observed in the HRTEM analysis (Fig. S6), while plenty of defects can easily be found in the cases of $WSe_{1.61}$/CNT and $WSe_{1.33}$/CNT (Fig. S7 and S8).

As host materials, WSe_{2-x}/CNT is loaded with sulfur by the melt diffusion method [33, 46]. In the prepared S/WSe_{2-x}/CNT materials, sulfur exists as monoclinic phase (XRD, Fig. S9). The sulfur content in all the four samples are almost equal (~72 wt%), and the detailed data are determined by Thermogravimetric Analysis (TGA) shown in Fig. S10. The S/WSe_{2-x}/CNT materials generally keep the original morphology of WSe_{2-x}/CNT (Fig. S11), and sulfur is homogeneously distributed in the host materials (Fig. S12).

2.2 Electrochemical performance of S/WSe_{2-x}/CNT

In the potential range of Li-S battery (1.7~2.8 V vs Li^+/Li), the WSe_{2-x}/CNT host materials are inactive and have negligible capacity contribution (Fig. S13). The batteries with S/$WSe_{1.96}$/CNT, S/$WSe_{1.61}$/CNT, S/$WSe_{1.51}$/CNT and S/$WSe_{1.33}$/CNT as the cathode were assembled to measure the electrochemical performances. Fig. S14 displays the CV curves of the cathodes at a scan rate of 0.05 mV s^{-1}. The peak shapes of S/$WSe_{1.51}$/CNT electrode are stronger than those of the other electrodes based on different defects materials, indicating faster kinetics of the S/$WSe_{1.51}$/CNT electrode. Compared with the S/$WSe_{1.96}$/CNT, S/$WSe_{1.61}$/CNT and S/$WSe_{1.33}$/CNT electrodes, the anodic peaks of S/$WSe_{1.51}$/CNT electrode shift to lower potentials in the charge sweep and the cathodic peaks of S/$WSe_{1.51}$/CNT electrode shift to higher potentials in the discharge sweep, indicating that the S/$WSe_{1.51}$/CNT electrode facilitates faster sulfur redox reactions and significantly faster kinetics for conversion reaction of polysulfides during cycling [33]. The initial charge-discharge curves in Fig. 3a show that S/$WSe_{1.51}$/CNT delivers the highest discharge capacity of 1345.9 mAh g^{-1} and the near-stoichiometric S/$WSe_{1.96}$/CNT provides the lowest value of 1053.7 mAh g^{-1} at 0.05C with a clear order: S/$WSe_{1.51}$/CNT > S/$WSe_{1.33}$/CNT > S/$WSe_{1.61}$/CNT > S/$WSe_{1.96}$/CNT. For S/$WSe_{1.51}$/CNT, the relatively low potential difference between charge and discharge means a low overpotential, related to a low activation energy in the catalytic electrode reaction. Obviously, the potential difference for the near-stoichiometric S/$WSe_{1.96}$/CNT is relatively high. Fig. 3b shows the cycle performance of the Li-S batteries with the different host materials. Remarkably, S/$WSe_{1.51}$/CNT shows an outstanding cycle performance, retaining a capacity of 886.1 mAh g^{-1} after 200 cycles at 0.2C with a coulombic efficiency of 99.3%, while 787.9 mAh g^{-1} for S/$WSe_{1.61}$/CNT, 680.7 mAh g^{-1} for S/$WSe_{1.33}$/CNT and 551.4 mAh g^{-1} for S/$WSe_{1.96}$/CNT. Therein, the capacity of S/$WSe_{1.33}$/CNT during the early tens of cycles is higher than that of S/$WSe_{1.61}$/CNT, but a faster capacity decay ocurrs, indicating a relatively poor cycling stability. The EIS analysis of S/$WSe_{1.33}$/CNT after 200 cycles reveals that the increase of charge transfer impedance and the larger resistance of the insoluble Li_2S_2/Li_2S layer

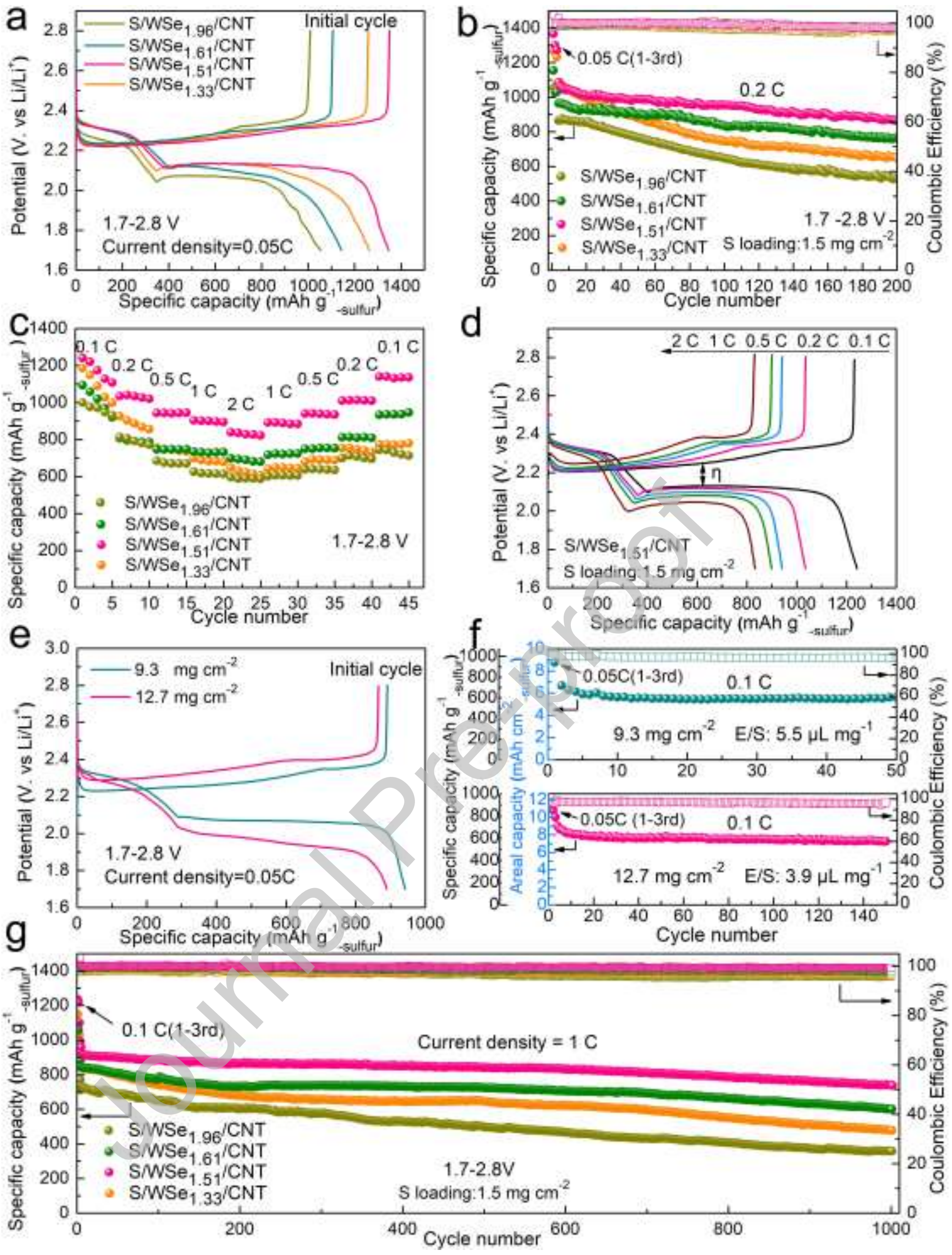

Fig. 3. Electrochemical performance of S/WSe$_{2\text{-}x}$/CNT. (a) The first charge and discharge curves at 0.05 C; (b) Cycling performance at 0.2 C (1-3rd for activation at 0.05 C); (c) evaluation of the rate capacities; (d) Charge-discharge curves at various rates for the S/WSe$_{1.51}$/CNT electrode; (e) The initial charge-discharge curves at 0.05 C and with sulfur loading of 9.3 and 12.7 mg cm^{-2}; (f) cycling performance of the lithium-sulfur cells with high sulfur loading and low E/S ratio; (g) Long cycling performances and coulombic efficiency at 1 C rate.

than S/$WSe_{1.61}$/CNT during cycling (Fig. S15, Table S3). Besides the advantages in capacity and cycle performance, S/$WSe_{1.51}$/CNT also has an excellent rate performance as shown in Fig. 3c. The average discharge capacity at 0.1, 0.2, 0.5, 1 and 2 C, are 1241.5, 1041, 944.8, 903.2, and 839.2 mAh g^{-1}, respectively. S/$WSe_{1.61}$/CNT and S/$WSe_{1.33}$/CNT have close rate performance, with ups and downs on both at various rates, but it is clear that the near-stoichiometric S/$WSe_{1.96}$/CNT is relatively poor. Moreover, with improving discharge rates, S/$WSe_{1.51}$/CNT presents a smaller potential drop which is calculated by subtracting the median potential at the midpoint of discharge capacity from the counterpart of charge curve, compared with the others (Fig. 3d, Fig. S16**)**. In particular, at 2C rate, S/$WSe_{1.51}$/CNT still deliveries the typical multi-step discharge profile of Li-S battery, however obviously increased overpotential appear as dotted in the Fig. S16. The long-cycle performance at 1C rate is also investigated, as shown in Fig. 3g and S17. As expected, S/$WSe_{1.51}$/CNT still shows the best cycle performance at the relatively high rate, and the discharge capacity after 1000 cycles are maintained at 741.4 mAh g^{-1} and the coulomb efficiency at the 1000th cycle is still up to 99.2% with fading rate per cycle only being 0.025% (based on the 4rd cycle). As comparison, the capacities of S/$WSe_{1.96}$/CNT, S/$WSe_{1.61}$/CNT and S/$WSe_{1.33}$/CNT after 1000 cycles are only 359.4, 602.5 and 478.1 mAh g^{-1}, respectively, with lower coulomb efficiency 95.9%, 97.6 and 96.8%, corresponding faster capacity decay rate of 0.053%, 0.032% and 0.048%, respectively. The electrochemical performances indicate clearly that there exists direct relation between the defects of WSe_{2-x} and the electrode reactions, and a moderate number of defects can help Li-S battery achieve an optimal electrochemical performance.

Even under harsh operating conditions i.g. lean electrolyte/sulfur ratio (E/S) and high sulfur areal loading, S/$WSe_{1.51}$/CNT still provides statisfied electrochemical performance. With increasing sulfur loading from 1.5 mg cm^{-2} to 9.3 and 12.7 mg cm^{-2}, and the corresponding E/S decreases to 5.5 and 3.9 μL mg^{-1}, respectively. Though the harsh conditions inevitably cause a light fall in initial capacity and discharge potential (Fig. 3e), the area capacity can maintain 5.6 mAh cm^{-2} (50 cycles) and 7.7 mAh cm^{-2} (150 cycles) at the current density of 0.1C (1-3 rd at 0.05C for activation of the thick electrodes), respectively (Fig. 3f), even to be stable at 0.15 C and 0.2 C (Fig. S18, S19). Compared to the similar reports containing typical 2D materials in recent years, this result is very encouraging (Fig. S20 and Table S4).

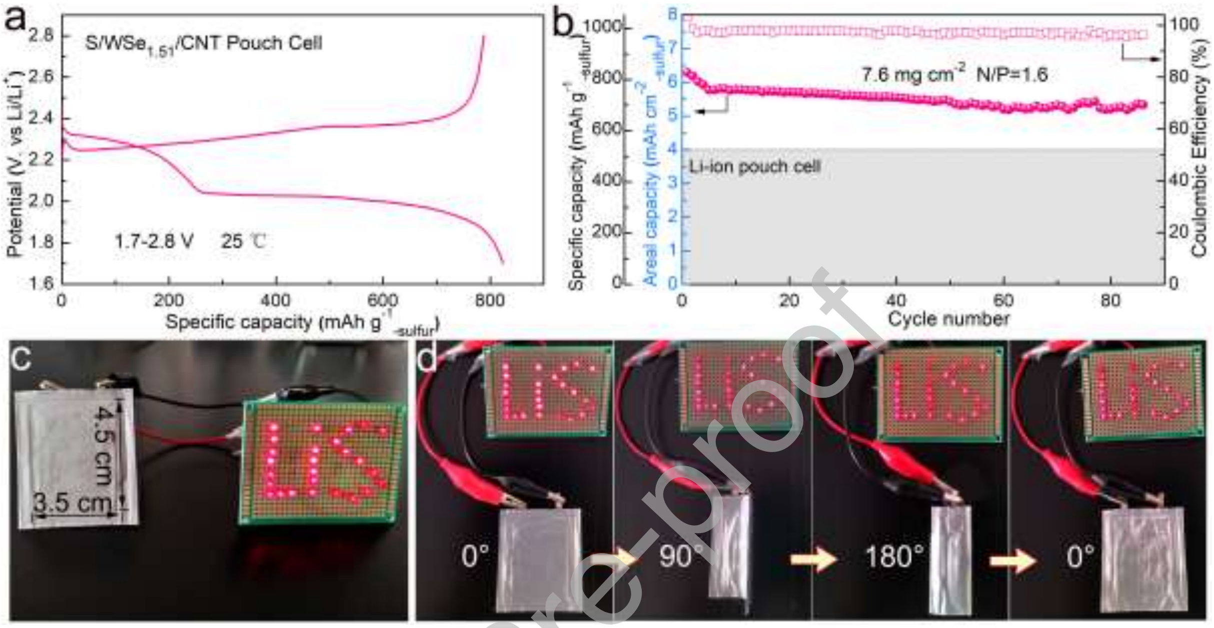

Fig. 4. Pouch cell performance of the S/$WSe_{1.51}$/CNT electrode. (a) First discharge-charge cycle; (b) cycling performance at room temperature; (c) photographs of an LED illumination test-driven by the assembled pouch cell of size; (d) photographs showing the ability of the pouch cells to empower LED under bending.

In addition, to further demonstrate the practical potential of S/$WSe_{1.51}$/CNT electrode, Fig. 4 shows the test for pouch cell. The loading sulfur is 7.6 mg cm^{-2}, and the contact area of the electrode is 15.75 cm^2 (3.5×4.5 cm; ratio of negative to positive, N/P=1.6). Fig. 4a and 4b shows that S/$WSe_{1.51}$/CNT still has a typical discharge-charge curve and stable cyclic capacity in pouch cell. After 86 cycles, S/$WSe_{1.51}$/CNT can still provide a capacity of 5.4 mAh cm^{-2} (with a current density of 0.05C and electrolyte to sulfur ratio E/S=10 μL mg^{-1}), which is significantly higher than that of commercial lithium-ion batteries (LIBS, 4.0 mAh cm^{-2}) (Fig. 4b). Moreover, the pouch cell provides continuous energy output despite a series of folding operations from 0° to 180° (Fig. 4d). Therefore, it can be further expected that S/$WSe_{1.51}$/CNT also has potential for practical application in Li-S batteries.

2.3 Effect mechanism of defects in WSe_{2-x} on electrochemcial performance

The cathode reaction of Li-S battery involves a complicated solid-liquid-solide phase multi-step process, in which the core steps include adsorption of polysulfides on the host and electron transfer under the catalytic effect of the host, in particular the precipitation process from soluble Li_2S_x to insoluble Li_2S_2 and Li_2S [30]. The adsorption ability of the WSe_{2-x}/CNT materials is firstly evaluated by the static adsorption experiment of Li_2S_6. The supernatant after adsorbed by WSe_{2-x}/CNT for 2 hours is separated and analyzed by UV-Vis adsorption spectroscopy (Fig. 5a, Fig. S21). Based on the analysis of lithium polysulfides in the UV-vis spectrum of Li_2S_6 etheryl solution, the ~350 nm absorption band are assigned to Li_2S_6 and LiS_6^-, the strong absorbance at ~420 nm is derived from LiS_6^-, and the band at ~620 nm is contributed by $LiS_3^{\bullet}$ radical [33, 47]. Interestingly, the intensity of the dominant band for Li_2S_6 shows gradient derease with increasing defects of WSe_{2-x}/CNT, convincingly demonstrating the defects can provide adsorption sites for polysulfides. The adsorption behavior is further studied by density functional calculations (DFT), and the modeling simulation details are listed in the Experimental Section. Fig. 5b presents the optimized configuration of Li_2S_6 on the (002) plane with the optimal configuration of 2D TMDs crystal. With the increase of defects from the near-stoichiometric $WSe_{1.96}$/CNT to $WSe_{1.33}$/CNT, the disorder degree of atomic arrangement of the configuration of (002) planes raises gradually. The change of atomic arrangement can affect the coupling interaction between WSe_{2-x} and Li_2S_6 which corresponds to the polar electrophilic bonding of S_x^{2-}-$W^{\delta+}$ and Li^+-$Se^{\delta-}$. On the near-stoichiometric $WSe_{1.96}$/CNT, the coupling interaction is dominantly from Li^+-$Se^{\delta-}$

bonding, and the bonding energy E_b= -0.17 eV. However, in the cases of the WSe_{2-x} with a number of defects, the atomic rearrangements

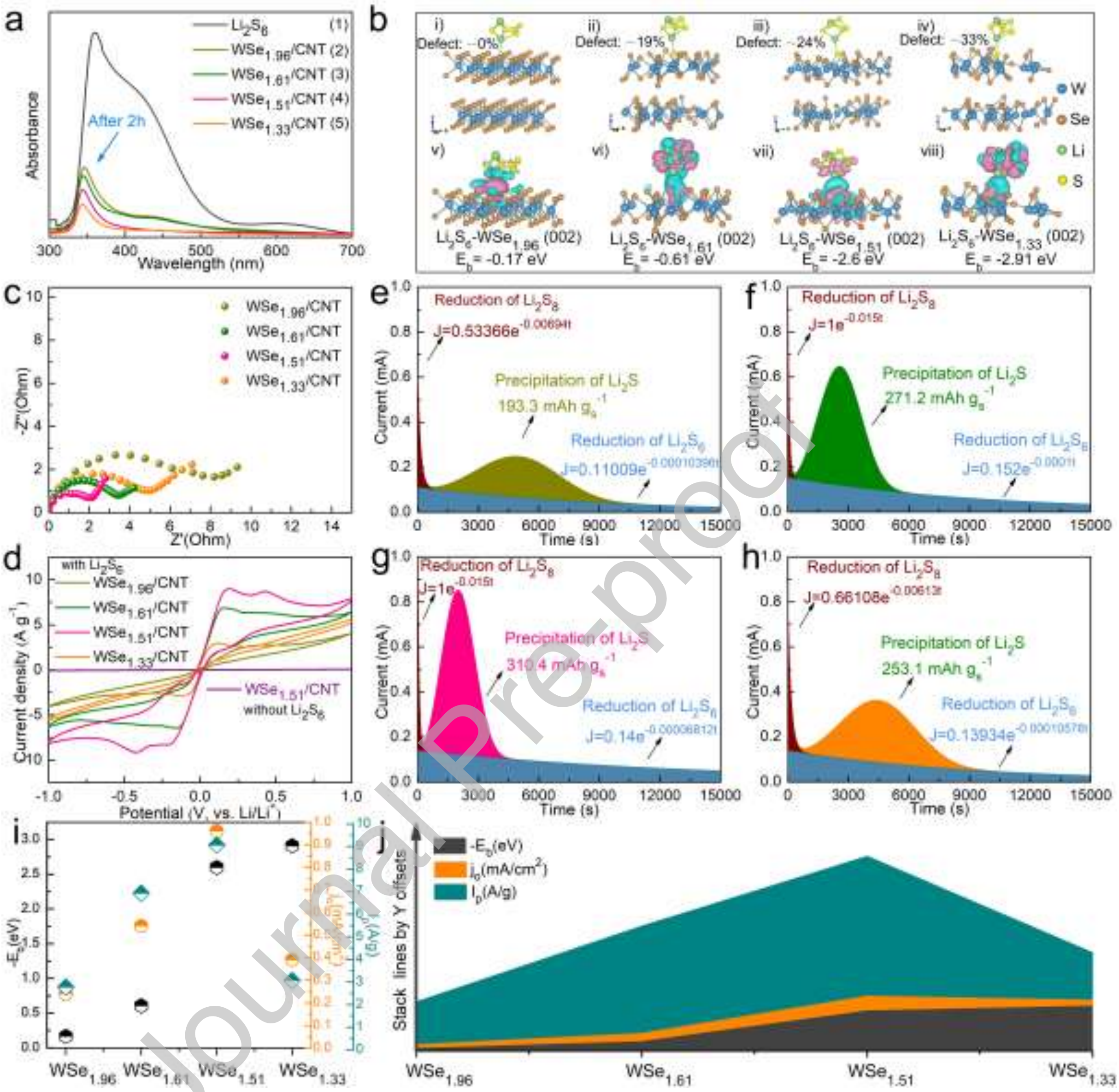

Fig. 5. Mechanism and kinetics. (a) UV-Vis spectra of the Li_2S_6 solution before and after static adsorption by WSe_{2-x}/CNT; (b) DFT calculation results of stable configurations (i-iv) and charge transfers (v-viii), where pink and cyan isosurface represent the spatial regions augmented and reduced charge densities, respectively; (c) EIS spectra of the symmetric configuration with various electrodes and Li_2S_6 solution; (d) CV curves of the symmetric configuration with Li_2S_6 solution; (e-h) potentiostatic discharge curves of Li_2S_8/tetraglyme solution at 2.0 V on various surfaces of WSe_{2-x}/CNT; (i) quantitative comparison of the electrochemical behavior based on results from (b, c, d) and the schematic showing in (j).

provide additional coupling interaction S_x^{2-}-$W^{\delta+}$ with stronger bonding energy (Fig. 5b(ii-iv)). Moreover, the bonding energy gradually increases with increasing defects, -0.61 eV for $WSe_{1.61}$, -2.6 eV for $WSe_{1.51}$, and -2.91 eV for $WSe_{1.33}$, respectively. The difference in the interactions is also shown visually by charge difference isosurface shown in Fig. 5b(v-viii). Different from Li^{+}-$Se^{\delta-}$, the bonding of S_x^{2-}-$W^{\delta+}$ means that electrons shift from the host materials to the adsorbed polysulfides, which is helpful for the electron transfer in the cathode reactions during discharging. To compare the charge disserence isofurface, it can be found that, in the case of $WSe_{1.51}$/CNT, the adsorbed polysufide presents improved charge density with sulfur, while increase and decrease coexist for sulfur atoms in the cases of $WSe_{1.61}$/CNT and $WSe_{1.33}$/CNT. This will make the polysulfides on $WSe_{1.51}$/CNT easier to capture lithium ions from the electrolyte to compelete the cathode reactions.

Charge transfer processes of polysulfides on WSe_{2-x}/CNT are further investigated by electrochemical impedance spectra (EIS) of the symmetric configuration with Li_2S_6 solution. As shown in Fig. 5c, the semicircle in the high-frequency region presents a descending order: $WSe_{1.96}$/CNT > $WSe_{1.33}$/CNT > $WSe_{1.61}$/CNT > $WSe_{1.51}$/CNT, indicating the effect of the defects on charge transfer impedance (R_{ct}) in the electrochemical process, and $WSe_{1.51}$ with a moderate number of defects has the lowest impedance for charge transfer [29, 43]. Generally the defects are beneficial for charge transfer in the electrochemical process. However, excessive defects could have negetive effect on electron transport of the material itself due to a large number of dislocations and structural distortions (Fig. S8c) [29, 48, 49]. Furthermore, the electrode process, especially catalytic ability, of the WSe_{2-x}/CNT samples are also investigated by cyclic voltammetry (CV). In Fig. 5d, the three cathodic peaks correspond the reduction processes from S_8 to S_6^{2-}(0.16 V), S_6^{2-} to S_4^{2-}(-0.19 V), and S_4^{2-} to Li_2S (-0.42 V), respectively; and the three anodic peaks are the oxidation processes from Li_2S to S_4^{2-} (-0.16 V), S_4^{2-} to S_6^{2-} (0.19 V), and S_6^{2-} to S_8 (0.42 V), respectively (Fig. S22) [33, 50]. As well known, the peak current density and peak sharpness can reflect catalytic ability for polysulfides of the host materals in the research of Li-S battery [51, 52]. Generally, the peak current density shows the same order as that from the EIS spectra, and $WSe_{1.51}$/CNT presents the optimal ability. Especially, the peak attributed to S_4^{2-} to Li_2S at -0.42 V and the one corresponding to S_6^{2-} to S_8 at 0.42 V in the case of $WSe_{1.51}$/CNT clearly suggest that $WSe_{1.51}$/CNT support a rapid catalytic redox process for the core steps of solid-liquid phase transformation.

Another key step in the cathode reaction is the liquid-solid phase conversion from soluble Li_2S_x to Li_2S_2 and Li_2S because the insolubility means a large energy barrier for nucleation and growth of Li_2S on host materials [53]. Therefore, the situation of Li_2S deposition on the host materials can reflect the key electrochemical process. The results in Fig. 5e-h show that the deposition amount and deposition time change following a consistent trend with the EIS analysis. The deposition amount of Li_2S increases gradually from $WSe_{1.96}$/CNT and $WSe_{1.61}$/CNT to $WSe_{1.51}$/CNT, but decreases in the case of $WSe_{1.33}$/CNT with excess defects. The calculated Li_2S conversion capacity for $WSe_{1.51}$/CNT is 310.4 mAh g^{-1}, higher than that of $WSe_{1.96}$/CNT(193.3 mAh g^{-1}), $WSe_{1.61}$/CNT(271.2 mAh g^{-1}) and $WSe_{1.33}$/CNT (253.1 mAh g^{-1}), on the basis of Faraday's law [54]. Moreover, $WSe_{1.51}$/CNT takes a shorter deposition time than the others, indicating a faster nucleation rate for Li_2S with a reduced energy barrier; this is exactly the essence of catalytic effect. To further evaluate the conversion ability of host materials, the initial activation energy barrier of Li_2S on various electrode materials was investigated (Fig. S23). Of note, the charge voltage plateaus after the short jump due to the phase conversion reaction from Li_2S to LiPSs [55]. Obviously, the S/$WSe_{1.51}$/CNT cathode displayed the lower potential barrier at about 2.276 V with a mild voltage jump peak than S/$WSe_{1.96}$/CNT (2.326 V), S/$WSe_{1.61}$/CNT (2.297 V) and S/$WSe_{1.33}$/CNT (2.311 V), indicating an accelerated activation process with low charge transfer barrier. And simultaneously, cyclic voltammetry (CV) testing at 0.05-0.3 mV s^{-1} rates were used to evaluate the lithium ion diffusion coefficient (Fig. S24). The corresponding fitted lines of peak current versus scan rate plots at cathodic/anodic peaks (named as C1, C2, A1, A2) [25]. The slopes of the hosts show linearly quantized value, which present an ascending order: $WSe_{1.96}$/CNT < $WSe_{1.33}$/CNT < $WSe_{1.61}$/CNT < $WSe_{1.51}$/CNT, suggesting the progressively enhanced lithium ion diffusion capability among these four hosts. It is a remarkable fact that the C2 peaks (at around 2.0 V) and the A1 peaks (at around 2.3 V) of the S/$WSe_{1.51}$/CNT, indicating the strongest redox kinetics of LiPSs to insoluble Li_2S and reverse process, respectively.

Summarizing the above results, the comprehensive performance of the WSe_{2-x} host materials can be quantitatively evaluated. Besides the adsorption ability represented by the bonding energy E_b, the catalytic ability of the host materials can be reflected by the exchange current density of a catalytic electrodes, j_0, which can be calculated by the following Equation (1) [56, 57]:

$$j_o = \frac{RT}{nFR_{ct}} \quad (1)$$

in which R is the gas content, T is the absolute temperature, n is the number of elements being transfered, F is the Faraday content, and R_{ct} is charge transfer impedance from the Fig. 5c. In addition, the peak current intensity I_p in the CV measurement is positively related to diffusion of the reactants in the interface of the host materials. Therefore, E_b, j_0, and I_p are summarized in Fig. 5i for comparison, and a stack lines by Y offsets is also illustrated as function of the amount of defects in WSe_{2-x} to more clearly show the comprehensive performance of the WSe_{2-x} host materials (Fig. 5j). Distinctly, the introduction of defects promotes all the three core parameters, the maximum value is achieved at the moderate number of defects for $WSe_{1.51}$, while excessive defects lead to a decreased comprehensive performance due to fall of catalytic ability though strong adsorption.

The defects and the crosslinked structure of WSe_{2-x}/CNT can be stably kept during charge-discharge cycles. After 200 cycles at 0.2C rate, the Li-S battery are disassemblied and the cathode is characterized. Fig. S25a, b demonstrate that the crosslinked structure of $WSe_{1.51}$/CNT has not obvious changes compared with the original. The HRTEM and IFFT pattern in Fig. S25c-f confirm that the hexagonal phase of WSe_{2-x}, Se atomic vacancies, and the dislocations are still maintained afther the long cycling, indicating the defects can sustainably play the important role for promoting the cathode reaction in Li-S batteries.

3. Conclusions

The defects of 2D few-layer tungsten selenide are quantitatively regulated by changing simply the preparation conditions. The added defects mainly include anionic Se vacancies and edge dislocations distributed dominantly in the basal plane of the 2D material. It is comfirmed that the defects in tungsten selenide are not only additional catalytically active sites for the conversion reactions of polysulfide immediaters for Li-S batteries, but also have strong catalytic ability due to the coupling interaction S_x^{2-}-$W^{\delta+}$. For the cathode reactions in Li-S batteries, the introducation of defects promotes the core steps like adsorption of polysulfides, charge transfer to polysulfides and liquid-solid phase conversion. However, excessive defects can cause the decrease of catalytic ability owing to transformation of defect site configuration. Among the WSe_{2-x} with defects regulated quantitively from the near-stoichiometric $WSe_{1.96}$ to $WSe_{1.33}$, $WSe_{1.51}$ shows the optimal performance. The S/$WSe_{1.51}$/CNT electrode delieveries the high areal capacity of 11.3 mAh cm^{-2} with a high sulfur loading of 12.7 mg cm^{-2}, and the excellent cycling stability with a decay rate of 0.025% during 1000 cycles at 1C. Additionally, the corresponding pouch cell shows foldable flexibility and a stable areal capacity of 5.4 mAh cm^{-2} with areal loading 7.6 mg cm^{-2}. It is encouraging approach that the generation of an appropriate proportion of defects in the dominant basal planes of 2D materials improves the catalytic ability to achieve a high-performance Li-S battery.

4. Experimental

4.1 Preparation

All chemicals were of analytical grade and used without further purification. The solvothermal and annealing method was used to prepare a series of tungsten selenide materials, similar to the previous reports [33, 43]. Firstly, carbon nanotubes (CNTs) were activated. 2 g CNTs was added in a round-bottom flask containing 60 mL concentrated nitric acid, and refluxed continuously at 130 ℃ for 12 h. After cooling to room temperature, CNTs were filtered and washed, and then dried in 60 ℃ for 24 h. To preparation of WSe_{2-x}/CNT, selenium powder (0.14 M), sodium borohydride ($NaBH_4$) (90 mM), and 0.05 g the activated CNTs were added in 60 mL N, N-dimethylformamide (DMF), and mixed ultrasonically for 0.5 h. Sodium tungstate ($Na_2WO_4·2H_2O$) (70 mM) was added and kept stirring for more 0.5 h. The obtained mixture was transferred into a 100 ml autoclave and kept at 220 ℃ for 24 h. After cooling to room temperature, the solid product was washed with deionized water and anhydrous ethanol for several times, and then vacuum freeze-dried for 24 h to obtain the precursor. To prepare WSe_{2-x}/CNT with defects regulated quantitively, the precursor was calcined for 3 h, in 500 ℃ with argon, in 500 ℃ with 5% hydrogen/argon, in 500 ℃ with 10% hydrogen/argon, and 600 ℃ with 10% hydrogen/argon, respectively, to obtain $WSe_{1.96}$/CNT, $WSe_{1.61}$/CNT, $WSe_{1.51}$/CNT, and $WSe_{1.33}$/CNT, in which the atomic ratio of W to Se was determined by ICP-OES.

Sulfur was loaded by a melt diffusion method. Firstly, the WSe_{2-x}/CNT host material and S were continuously ground for 0.5 h according to the mass ratio of 28:72, then transferred in an argon-filled autoclave and heated at 155 ℃ for 12 h.

4.2 Characterization

Morphology and microstructure of the materials were characterized by scanning electron microscopy (SEM, JSM-7800F) and transmission electron microscopy (TEM, JEM-2800). The X-ray diffraction (XRD) analysis was carried out with a Rigaku Smart Lab (3kW). The Raman spectra were collected by a Microconfocal Raman Spectrometer (SR-500I-A) with a 532 nm laser and a power of the laser ≥100 mW. Nitrogen adsorption was used to determine specific surface area with the Brunauer-Emmet-Teller (BET) model, and pore size distribution with BJH method (JW-BK112 Instrument). Sulfide content was determined on a thermogravimetric analyzer (Mettler Toledo, TGA/DSC) in the range of 30-800°C in argon with a temperature rate of 10° C min^{-1}. Element chemical state was analyzed by X-ray Photoelectron Spectroscopy (XPS, Escalab 250XI, Thermo Scientific) with Al Kα source. Electron Spin Resonance (ESR) spectra were measured on a Bruker A300 machine. A Vario MICRO Element Analysis Instrument was used to determine carbon content and Inductively Coupled Plasma Optical Emission Spectroscopy (ICP-OES, Agilent 5110 ICP-OES) measured the content of W and Se elements.

4.3 Electrochemical Measurements

To prepare sulfur cathode, WSe_{2-x}/CNT, conductive agent (Super-P) and polyvinylidene chloride (PVDF) were ground for 0.5 h at the weight proportion of 8:1:1, and soaked in N-methylpyrrolidone (NMP) with stirring to obtain a uniform slurry. The slurry was coated on aluminum foil containing carbon and dried at 60 °C for 24 h. Finally, the electrode plates with sulfur loading of 1.1-1.5 mg cm^{-2} and diameter of 10 mm were prepared for the routine electrochemical measurements. For the high sulfur loading of 9.3-12.7 mg cm^{-2}, the same methods were used except for carbon cloth as the current collector. Using Celgard 2325 as a separator and lithium foil (with a diameter of 14 mm and thick of 0.7 mm) as a counter electrode, the Type 2032 coin cells were assembled in a glove box filled with argon gas. The electrolyte was made of 1.0 M lithium bis(trifluoromethanesulfonyl)imide (LiTFSI) and 0.2 M lithium nitrate ($LiNO_3$) additives, in 1, 2-dimethoxyethane (DME) and 1,3-dioxolane

(DOL) (V/V, 1:1). The ratio of electrolyte to sulfur (E/S) was controlled at 10 μL mg^{-1} in the routine tests, and 5.5, 5.3, 4.8 and 3.9 μL mg^{-1} in high sulfur loading experiments. The charge/discharge measurements were carried out on a LAND-CT2001A instrument with a voltage window of 1.7-2.8 V (vs. Li^+/Li). Cyclic voltammetry (CV) measurements were made on the CHI600E electrochemical workstation with a scanning rate of 0.1 mV s^{-1} and a voltage range of 1.7 to 2.8 V. Electrochemical Impedance Spectra (EIS) were performed on a Zahner IM6EX electrochemical workstation with frequency ranging from 10 mHz to 100 kHz.

4.4 Polysulfide absorption

Li_2S_6 was selected as the indicator of polysulfides. 1 M of Li_2S_6 was prepared by the configuration of Li_2S and sulfur stoichiometry (5:1) in DOL/DME (V/V, 1:1) mixed solvent with a continuous stirring at 60°C for 48 h. 45 mg WSe_{2-x}/CNT was added into 5 mL of solution (diluting to 2 mM with DME), respectively. After static settlement for 2 h, the supernatant was separated and charaterized using a Ultraviolet Visible Spectrometer (UV-vis, Varian Cary 100 Conc). All the tests were performed in a glove box filled with argon gas.

4.5 Deposition of Li_2S

0.5 M Li_2S_8 solution was prepared by adding Li_2S and S (molar ratio of 1:7) into Tetraglyme containing 1.0 M LiTFSI. WSe_{2-x}/CNT (1 mg cm^{-2}) was used as work electrode and lithium foil as counter electrode. 20 μL Li_2S_8 electrolyte was added to the work electrode side and 20 μL contrast electrolyte without Li_2S_8 was added to the counter electrode side. Firstly, it was discharged to 2.06 V at 0.03 C, and then discharged at 2.0 V at LK2005 workstation until the current was lower than 10^{-5}A to nucleate Li_2S.

4.6 Computational Details

The model simulation was implemented in Vienna Ab-initio simulation package (VASP) [58] using the projector augmented wave (PAW) method [59]. The generalized gradient approximation (GGA) based on Perdew Burke Ernzerhof (PBE) parameterization scheme was used to optimize the structure [60]. In order to simulate the adsorption ability of the (002) plane, a slab model was constructed, containing 96 atoms (before deducting defects) and a 15Å vacuum layer. For all surface calculations, the Se atoms in the bottom layer are fixed and the other atoms were allowed to move. The Brillouin zone was sampled with a 3×3×1 Monkhorst-Pack grid k-points and the cutoff energy id set was to be 450 eV [61]. The structures were optimized until the Hellmann-Feynman forces on each atom were less than 0.02 eV/A. When the energy difference between subsequent iterations being less than 1×10^{-5} eV, the system energy was considered to be converged. The adsorption energy was calculated as $E_{ad}=E_{tot}-E_{Li2S6}-E_{(002-x)}$. In the equation, E_{tot} was the total energy of Li_2S_6 in the substrate with different vacancy sites and E_{Li2S6} was the energy of Li_2S_6. $E_{(002-x)}$ (x = 0, 19, 24, 33) was the energy of the substrate with varying amounts of vacancy sites, where x means the quantity of the vacancy sites.

Supporting Information

Supporting Information is available from the online version or from the author.

CRediT authorship contribution statement

Haojie Li: Experimental Design, Methodology, Writing-Original Paper Draft Preparation. **Kai Xi**: Methodology, Writing Logic Discussion. **Wei Wang**: Methodology. **Sheng Liu**: Formal analysis. **Xue-Ping Gao**: Formal analysis. **Guo-Ran Li**: Conceptualization, Resources, Writing-review & editing, Supervision.

Conflicts of interest

The authors declare that they have no known competing financial interests or personal relationships that could have appeared to influence the work reported in this paper.

Acknowledgements

Financial supports from the National Key Research and Development Program (2016YFB0100200) and National Natural Science Foundation of China (21935006) of China are gratefully acknowledged.

Notes and references

[1] P.G. Bruce, S.A. Freunberger, L.J. Hardwick, J.M. Tarascon, Li-O_2 and Li-S batteries with high energy storage, Nat. Mater. 11 (2012) 19-29.

[2] Q. Pang, A. Shyamsunder, B. Narayanan, C.Y. Kwok, L.A. Curtiss, L.F. Nazar, Tuning the electrolyte network structure to invoke quasi-solid state sulfur conversion and suppress lithium dendrite formation in Li–S batteries, Nat. Energy 3 (2018) 783-791.

[3] Y. Gao, Q. Guo, Q. Zhang, Y. Cui, Z. Zheng, Fibrous Materials for Flexible Li–S Battery, Adv. Energy Mater. 11 (2020) 2002580.

[4] Y.T. Liu, Y. Elias, J.S. Meng, D. Aurbach, R.Q. Zou, D.G. Xia, Q.Q. Pang, Electrolyte solutions design for lithium-sulfur batteries, Joule 5 (2021) 2323-2364.

[5] Y.C. Jiang, H.M.U. Arshad, H.J. Li, S. Liu, G.R. Li, X.P. Gao, Crystalline Multi-Metallic Compounds as Host Materials in Cathode for Lithium-Sulfur Batteries, Small 17 (2021) 2005332.

[6] Y. Jin, K. Liu, J.L. Lang, X. Jiang, Z.K. Zheng, Q.H. Su, Z.Y. Huang, Y.Z. Long, C.A. Wang, H. Wu, Y. Cui, High-Energy-Density Solid-Electrolyte-Based Liquid Li-S and Li-Se Batteries, Joule 4 (2020) 262-274.

[7] H. Zhang, L. Yang, P.G. Zhang, C.J. Lu, D.W. Sha, B.Z. Yan, W. He, M. Zhou, W. Zhang, L. Pan, Z.M. Sun, MXene-Derived Ti_nO_{2n-1} Quantum Dots Distributed on Porous Carbon Nanosheets for Stable and Long-Life Li-S Batteries: Enhanced Polysulfide Mediation via Defect Engineering, Adv. Mater. 33 (2021) 2008447.

[8] Y.C. Chien, A.S. Menon, W.R. Brant, D. Brandell, M.J. Lacey, Simultaneous Monitoring of Crystalline Active Materials and Resistance Evolution in Lithium-Sulfur Batteries, J. Am. Chem. Soc. 142 (2020) 1449-1456.

[9] X.J. Gao, X.F. Yang, M.S. Li, Q. Sun, J.N. Liang, J. Luo, J.W. Wang, W.H. Li, J.W. Liang, Y.L. Liu, S.Z. Wang, Y.F. Hu, Q.F. Xiao, R. Li, T.K. Sham, X.L. Sun, Cobalt-Doped SnS_2 with Dual Active Centers of Synergistic Absorption-Catalysis Effect for High-S Loading Li-S Batteries, Adv. Funct. Mater. 29 (2019) 1806724.

[10] Z. Sun, S. Vijay, H.H. Heenen, A.Y.S. Eng, W. Tu, Y. Zhao, S.W. Koh, P. Gao, Z.W. Seh, K. Chan, H. Li, Catalytic Polysulfide Conversion and Physiochemical Confinement for Lithium–Sulfur Batteries, Adv. Energy Mater. 10 (2020) 1904010.

[11] W.B. Kong, L.J. Yan, Y.F. Luo, D.T. Wang, K.L. Jiang, Q.Q. Li, S.S. Fan, J.P. Wang, Ultrathin MnO_2/Graphene Oxide/Carbon Nanotube Interlayer as Efficient Polysulfide-Trapping Shield for High-Performance Li-S Batteries, Adv. Funct. Mater. 27 (2017) 1606663.

[12] X. Liu, J.Q. Huang, Q. Zhang, L. Mai, Nanostructured Metal Oxides and Sulfides for Lithium-Sulfur Batteries, Adv. Mater. 29 (2017) 1601759.

[13] J. Yu, J.W. Xiao, A.R. Li, Z. Yang, L. Zeng, Q.F. Zhang, Y.J. Zhu, and L. Guo, Enhanced Multiple Anchoring and Catalytic Conversion of Polysulfides by Amorphous MoS_3 Nanoboxes for High-Performance Li-S Batteries, Angew. Chem. Int. Ed. 59 (2020) 13071.

[14] J.R. He, A. Bhargav, H.Y. Asl, Y.F. Chen, M. Arumugam, 1T′-ReS_2 Nanosheets In Situ Grown on Carbon Nanotubes as a Highly Efficient Polysulfide Electrocatalyst for Stable Li–S Batteries, Adv. Energy Mater. 10 (2020) 2001017.

[15] S. Manzeli, D. Ovchinnikov, D. Pasquier, O.V. Yazyev, A. Kis, 2D transition metal dichalcogenides, Nat. Rev. Mater. 2 (2017) 17033.

[16] A. Eftekhari, Tungsten dichalcogenides (WS_2, WSe_2, and WTe_2): materials chemistry and applications, J. Mater. Chem. A 5 (2017) 18299-18325.

[17] H.J. Li, Q.M. Su, J.W. Kang, H.G. Feng, P. Huang, M. Feng, M. Huang, G.H. Du, Fabrication of MoS_2@SnO_2-SnS_2 composites and their applications as anodes for lithium ion batteries, Mater. Res. Bull. 108 (2018) 106-112.

[18] P. Chen, W.W. Pai, Y.H. Chan, W.L. Sun, C.Z. Xu, D.S. Lin, M.Y. Chou, A.V. Fedorov, T.C. Chiang, Large quantum-spin-Hall gap in single-layer 1T' WSe_2, Nat. Commun. 9 (2018) 2003.

[19] X.Q. Song, D. Tian, Y. Qiu, X. Sun, B. Jiang, C.H. Zhao, Y. Zhang, L.S. Fan, N.Q. Zhang, Improving poisoning resistance of electrocatalysts via alloying strategy for high-performance lithium-sulfur batteries, Energy Storage Mater. 41 (2021) 248-254.

[20] L. Chen, B.L. Liu, A.N. Abbas, Y.Q. Ma, X. Fang, Y.H. Liu, C.W. Zhou, Screw-Dislocation-Driven Growth of Two-Dimensional Few-Layer and Pyramid-like WSe_2 by Sulfur-Assisted Chemical Vapor Deposition, ACS Nano 8 (2014) 11543-11551.

[21] X. Xiao, H. Wang, W.Z. Bao, P. Urbankowski, L. Yang, Y. Yang, K. Maleski, L.F. Cui, S.J.L. Billinge, G.X. Wang, Y. Gogotsi, Two-Dimensional Arrays of Transition Metal Nitride Nanocrystals, Adv. Mater. 31 (2019) 1902393.

[22] B. Lei, G.R. Li, X.P. Gao, Morphology dependence of molybdenum disulfide transparent counter electrode in dye-sensitized solar cells, J. Mater. Chem. A 2 (2014) 3919-3925.

[23] T. Yang, J. Zhou, T.T. Song, L. Shen, Y.P. Feng, M. Yang, High-Throughput Identification of Exfoliable Two-Dimensional Materials with Active Basal Planes for Hydrogen Evolution, ACS Energy Lett. 5 (2020) 2313-2321.

[24] Y. Sun, X.W. Zhang, B.G. Mao, M.H. Cao, Controllable selenium vacancy engineering in basal planes of mechanically exfoliated WSe_2 monolayer nanosheets for efficient electrocatalytic hydrogen evolution, Chem. Commun. 52 (2016) 14266-14269.

[25] Y.K. Wang, R.F. Zhang, J. Chen, H. Wu, S.Y. Lu, K. Wang, H.L. Li, C.J. Harris, K. Xi, R.V. Kumar, S.J. Ding, Enhancing Catalytic Activity of Titanium Oxide in Lithium–Sulfur Batteries by Band Engineering, Adv. Energy Mater. 9 (2019) 1900953.

[26] M. Tosun, L. Chan, M. Amani, T. Roy, G.H. Ahn, P. Taheri, C. Carraro, J.W. Ager, R. Maboudian, A. Javey, Air-Stable n-Doping of WSe_2 by Anion Vacancy Formation with Mild Plasma Treatment, ACS Nano 10 (2016) 6853-6860.

[27] X.S. Sun, X. Luo, X.D. Zhang, J.F. Xie, S. Jin, H. Wang, X.S. Zheng, X.J. Wu, Y. Xie, Enhanced Superoxide Generation on Defective Surfaces for Selective Photooxidation, J. Am. Chem. Soc. 141 (2019) 3797-3801.

[28] Z.X. Shi, M. Li, J.Y. Sun, Z.W. Chen, Defect Engineering for Expediting Li–S Chemistry: Strategies, Mechanisms, and Perspectives, Adv. Energy Mater. 122 (2021) 2100332.

[29] B. Wang, J.W. Liu, S. Yao, F.Y. Liu, J.Q. He, Y.K. Li, Z. Lin, F. Huang, c. liu, M.Y. Wang, Vacancy Engineering in Nanostructured Semiconductors for Enhancing Photocatalysis, J. Mater. Chem. A (2021) 17143-17172.

[30] Z. Zhang, D. Luo, G.R. Li, R. Gao, M. Li, S. Li, L. Zhao, H.Z. Dou, G.B. Wen, S. Sy, Y.F. Hu, J.D. Li, A.P. Yu, Z.W. Chen, Tantalum-Based Electrocatalyst for Polysulfide Catalysis and Retention for High-Performance Lithium-Sulfur Batteries, Matter 3 (2020) 920-934.

[31] D. Luo, Z. Zhang, G.R. Li, S.B. Cheng, S. Li, J.D. Li, R. Gao, M. Li, S. Sy, Y.P. Deng, Y. Jiang, Y.F. Zhu, H.Z. Dou, Y.F. Hu, A.P. Yu, Z.W. Chen, Revealing the Rapid Electrocatalytic Behavior of Ultrafine Amorphous Defective Nb_2O_{5-x} Nanocluster toward Superior Li-S Performance, ACS Nano 14 (2020) 4849-4860.

[32] H.B. Lin, L.Q. Yang, X. Jiang, G.C. Li, T.R. Zhang, Q.F. Yao, G.Y.W. Zheng, J.Y. Lee, Electrocatalysis of polysulfide conversion by sulfur-deficient MoS_2 nanoflakes for lithium–sulfur batteries, Energy Environ. Sci. 10 (2017) 1476-1486.

[33] H.J. Li, Y.H. Song, K. Xi, W. Wang, S. Liu, G.R. Li, X.P. Gao, Sulfur vacancies in Co_9S_{8-x}/N-doped graphene enhancing the electrochemical kinetics for high-performance lithium–sulfur batteries, J. Mater. Chem. A 9 (2021) 10704-10713.

[34] S. Zhang, S. Cao, T. Zhang, J.Y. Lee, Plasmonic Oxygen-Deficient TiO_{2-x} Nanocrystals for Dual-Band Electrochromic Smart Windows with Efficient Energy Recycling, Adv. Mater. 32 (2020) 2004686.

[35] D. Luo, G.R. Li, Y.P. Deng, Z. Zhang, J.D. Li, R.L. Liang, M. Li, Y. Jiang, W.W. Zhang, Y.S. Liu, W. Lei, A.P. Yu, Z.W. Chen, Synergistic Engineering of Defects and Architecture in Binary Metal Chalcogenide toward Fast and Reliable Lithium–Sulfur Batteries, Adv. Energy Mater. 9 (2019) 1900228.

[36] G. Wang, C. Robert, A. Suslu, B. Chen, S.J. Yang, S. Alamdari, I.C. Gerber, T. Amand, X. Marie, S. Tongay, B. Urbaszek, Spin-orbit engineering in transition metal dichalcogenide alloy monolayers, Nat. Commun. 6 (2015) 10110.

[37] Z.Y. Zhu, Y.C. Cheng, U. Schwingenschlögl, Giant spin-orbit-induced spin splitting in two-dimensional transition-metal dichalcogenide semiconductors, Phys. Rev. B 84 (2011) 153402.

[38] X.Q. Wang, Y.F. Chen, B.J. Zheng, F. Qi, J.R. He, Q. Li, P.J. Li, W.L. Zhang, Graphene-like WSe_2 nanosheets for efficient and stable hydrogen evolution, J. Alloy. Compd. 691 (2017) 698-704.

[39] X.Q. Wang, J.R. He, B.J. Zheng, W.L. Zhang, Y.F. Chen, Few-layered WSe_2 in-situ grown on graphene nanosheets as efficient anode for lithium-ion batteries, Electrochim. Acta 283 (2018) 1660-1667.

[40] X. Luo, Y.Y. Zhao, J. Zhang, M.L. Toh, C. Kloc, Q.H. Xiong, S.Y. Quek, Effects of lower symmetry and dimensionality on Raman spectra in two-dimensional WSe_2, Phys. Rev. B 88 (2013) 195313.

[41] P. Tonndorf, R. Schmidt, X.Y. Zhang, J. Börner, A. Liebig, M. Albrecht, C. Kloc, O. Gordan, D.R.T. Zahn, S.M.d. Vasconcellos, R. Bratschitsch, Photoluminescence emission and Raman response of monolayer MoS_2, $MoSe_2$, and WSe_2, OPT. EXPRESS 21 (2013) 4908.

[42] P. Pachfule, D. Shinde, M. Majumder, Q. Xu, Fabrication of carbon nanorods and graphene nanoribbons from a metal-organic framework, Nat. Chem. 8 (2016) 718–724.

[43] Y. Tian, G.R. Li, Y.G. Zhang, D. Luo, X. Wang, Y. Zhao, H. Liu, P.G. Ji, X.H. Du, J. Li, Z.W. Chen, Low-Bandgap Se-Deficient Antimony Selenide as a Multifunctional Polysulfide Barrier toward High-Performance Lithium-Sulfur Batteries, Adv. Mater. 32 (2020) 1904876.

[44] H.N. Ci, J.S. Cai, H. Ma, Z.X. Shi, G. Cui, M.L. Wang, J. Jin, N. Wei, C. Lu, W. Zhao, J.Y. Sun, Z.F. Liu, Defective VSe_2-Graphene Heterostructures Enabling In Situ Electrocatalyst Evolution for Lithium-Sulfur Batteries, ACS Nano 14 (2020) 11929-11938.

[45] J. Li, S. Han, J. Zhang, J. Xiang, X. Zhu, P. Liu, X. Li, C. Feng, B. Xiang, M. Gu, Synthesis of three-dimensional free-standing WSe_2/C hybrid nanofibers as anodes for high-capacity lithium/sodium ion batteries, J. Mater. Chem. A 7 (2019) 19898-19908.

[46] Y. Jeon, J. Lee, H. Jo, H. Hong, L.Y.S. Lee, Y. Piao, Co/Co_3O_4-embedded N-doped hollow carbon composite derived from a bimetallic MOF/ZnO Core-shell template as a sulfur host for Li-S batteries, Chem. Eng. J. 407 (2021) 126967.

[47] B.H. Zhang, J.F. Wu, J.K. Gu, S. Li, T.Y. Yan, X.P. Gao, The Fundamental Understanding of Lithium Polysulfides in Ether-Based Electrolyte for Lithium–Sulfur Batteries, ACS Energy Lett. 6 (2021) 537-546.

[48] J. Zhang, C.Y. You, H.Z. Lin, J. Wang, Electrochemical kinetics modulators in lithium sulfur batteries: from defect-rich catalysts to single atomic catalysts, Energy Environ. Mater. (2021) 10.1002/eem2.12250.

[49] W. Liu, C. Luo, S. Zhang, B. Zhang, J. Ma, X. Wang, W. Liu, Z. Li, Q.H. Yang, W. Lv, Cobalt-Doping of Molybdenum Disulfide for Enhanced Catalytic Polysulfide Conversion in Lithium-Sulfur Batteries, ACS Nano 15 (2021) 7491-7499.

[50] H.B. Lin, S.L. Zhang, T.R. Zhang, S. Cao, H.L. Ye, Q.F. Yao, G.W.W. Zheng, J.Y. Lee, A Cathode-Integrated Sulfur-Deficient Co_9S_8 Catalytic Interlayer for the Reutilization of "Lost" Polysulfides in Lithium-Sulfur Batteries, ACS Nano 13 (2019) 7073-7082.

[51] M.E. Pam, S. Huang, S. Fan, D. Geng, D. Kong, S. Chen, M. Ding, L. Guo, L.K. Ang, H.Y. Yang, Interface engineering by atomically thin layer tungsten disulfide catalyst for high performance Li–S battery, Mater. Today Energy 16 (2020) 100380.

[52] Z.Z. Du, X.J. Chen, W. Hu, C.H. Chuang, S. Xie, A. Hu, W.S. Yan, X.H. Kong, X.J. Wu, H.X. Ji, L.J. Wan, Cobalt in Nitrogen-Doped Graphene as Single-Atom Catalyst for High-Sulfur Content Lithium-Sulfur Batteries, J. Am. Chem. Soc. 141 (2019) 3977-3985.

[53] L. Peng, Z. Wei, C.Z. Wan, J. Li, Z. Chen, D. Zhu, D. Baumann, H. Liu, C.S. Allen, X. Xu, A.I. Kirkland, I. Shakir, Z. Almutairi, S. Tolbert, B. Dunn, Y. Huang, P. Sautet, X.F. Duan, A fundamental look at electrocatalytic sulfur reduction reaction, Nat. Catal. 3 (2020) 762-770.

[54] J.N. Wang, S.S. Yi, J.W. Liu, S.Y. Sun, Y.P. Liu, D.W. Yang, K. Xi, G.X. Gao, A. Abdelkader, W. Yan, S.J. Ding, K.R. Vasant, Suppressing the Shuttle Effect and Dendrite Growth in Lithium-Sulfur Batteries, ACS Nano 14 (2020) 9819-9831.

[55] S.Z. Wang, S.P. Feng, J.W. Liang, Q.M. Su, F.P. Zhao, H.J. Song, M. Zheng, Q. Sun, Z.X. Song, X.H. Jia, J. Yang, Y. Li, J.X. Liao, R.Y. Li, X.L. Sun, Insight into MoS_2–MoN Heterostructure to Accelerate Polysulfide Conversion toward High-Energy-Densit Lithium–Sulfur Batteries, Adv. Energy Mater. 11 (2021) 2003314.

[56] G.R. Li, X.P. Gao, Low-Cost Counter-Electrode Materials for Dye-Sensitized and Perovskite Solar Cells, Adv. Mater. 32 (2020) 1806478.

[57] M. Kouhnavard, N.A. Ludin, B.V. Ghaffari, K. Sopian, S. Ikeda, Carbonaceous materials and their advances as a counter electrode in dye-sensitized solar cells: challenges and prospects, ChemSusChem 8 (2015) 1510-33.

[58] G. Kresse, J. Furthmüller, Efficient iterative schemes for ab initio total-energy calculations using a plane-wave basis set, Phys. Rev. B 54 (1996) 11169-11186.

[59] P.E. Blochl, Projector augmented-wave method, Phys. Rev. B 50 (1994) 17953-17979.

[60] J.P. Perdew, K. Burke, M. Ernzerhof, Generalized gradient approximation made simple, Phys. Rev. Lett. 77 (1996) 3865-3868.

[61] H.J. Monkhorst, J.D. Pack, Special points for Brillouin-zone integrations, Phys. Rev. B 13 (1976) 5188-5192.

Graphical Abstract

A little wind kindles, much puts out the fire: Controlling the level of the in-plane defects in 2D tungsten selenide enhances their catalytic ability and promote the polysulfide conversion, leading to high-performance lithium-sulfur rechargeable battery.

Quantitatively Regulating Defects of 2D Tungsten Selenide to Enhance Catalytic Ability for Polysulfide Conversion in a Lithium Sulfur Battery